

DYNAMIC TOPOLOGICAL DATA ANALYSIS OF FUNCTIONAL HUMAN BRAIN NETWORKS

MOO K. CHUNG^{✉1} AND SOUMYA DAS^{✉*1} AND HERNANDO OMBAO^{✉2}

¹University of Wisconsin-Madison, USA

²King Abdullah University of Science and Technology, Saudi Arabia

ABSTRACT. Developing reliable methods to discriminate different transient brain states that change over time is a key neuroscientific challenge in brain imaging studies. Topological data analysis (TDA), a novel framework based on algebraic topology, can handle such a challenge. However, existing TDA has been somewhat limited to capturing the static summary of dynamically changing brain networks. We propose a novel dynamic-TDA framework that builds persistent homology over a time series of brain networks. We construct a Wasserstein distance based inference procedure to discriminate between time series of networks. The method is applied to the resting-state functional magnetic resonance images of human brain. We demonstrate that our proposed dynamic-TDA approach can distinctly discriminate between the topological patterns of male and female brain networks. MATLAB code for implementing this method is available at <https://github.com/laplcebeltrami/PH-STAT>.

1. Introduction. The dynamical changes in brain function and activity are an archetypal example of complex systems. Within this system, brain functions depend on constant interplays between local information processing and efficient global integration of information [64, 14, 25]. To reveal the underpinnings of neurodegenerative diseases, it is critical to analyze such interactions in brain pathology [70, 71, 39]. In brain network analysis, the neural interactions are encoded as a graph consisting of nodes and edges. Often, the whole brain is parcellated into several disjoint regions, which represented as network nodes [69, 26, 37, 32, 4] whereas the correlations between different parcellations (nodes) are represented as edge weights. In most analysis based on graph theory, features such as node degrees and clustering coefficients are acquired from adjacency matrices after thresholding edge weights [63, 79]. However, this leads to final statistical results and interpretations that rely on the choice of the threshold [44, 20] - which is subjective. Given this limitation, developing a multiscale network model that yields reliable outcomes independent of threshold choice is essential. Topological data analysis (TDA) can fill this gap by providing a topologically consistent solution across varying thresholds [29, 84, 59, 34, 18, 78]. Within TDA, persistent homology based approaches have become increasingly popular as a tool for analyzing different brain imaging data because they can capture the persistences [51, 60] of different topological features that are robust under different scales [13, 34, 44, 22]. The persistences are usually summarized and expressed using barcodes and persistence diagrams [61]. Although such approaches have been applied to increasingly diverse biomedical problems, they are mostly limited to investigating the *static* summary of *dynamically changing*

2020 *Mathematics Subject Classification.* Primary: 55N31, 62P10; Secondary: 37M10.

Key words and phrases. topological data analysis, persistent homology, brain networks, resting-state fMRI, time delay embedding.

data such as functional magnetic resonance images (fMRI) and electroencephalography (EEG) [21, 5, 77]. A recent development involves the application of TDA to analyze dynamic patterns in various datasets, including financial data [35] and gene expression data [53, 60].

Motivated by these studies, we develop a novel dynamic-TDA based approach that can statistically discriminate between two groups of brain networks, reflecting the dynamic nature of brain functional processes. This dynamic-TDA framework builds persistent homology over a multivariate time series [60] and constructs a test statistic using the Wasserstein distance between persistence diagrams. Our proposed dynamic-TDA, when applied to resting-state fMRI (rs-fMRI) data, reveals notable topological differences in the temporal dynamics between male and female subjects. This approach moves beyond the traditional methods that focus on static summaries of dynamic images [21, 5, 77], allowing for a more nuanced exploration of dynamic patterns within the images [35, 53, 60]. Motivated by time-delay embedding (TDE), we introduce a novel Dynamic Embedding technique to capture the temporal evolution of topological changes in multivariate time series data [76].

2. Methods. Human brain functional networks can be modeled as graphs, with nodes representing parcellated brain regions and edges indicating interactions between these regions [22]. We construct graph filtrations on these networks as described below. During this filtration process, topological features such as connected components (0-dimensional homology) and cycles (1-dimensional homology) emerge and vanish. A feature that appears at a filtration value b_i and disappears at d_i is represented as a point (b_i, d_i) in the plane. The set of all such points forms the persistent diagram (PD), which encapsulates the topology of the underlying network. When these features are represented as a collection of intervals on the real line, they constitute barcodes [17].

2.1. Graph filtration. Let $G = (V, W)$ be a weighted graph, where V is a set of nodes and W is the set of edge weights. The edge weight w_{ij} between nodes i and j are assumed to be unique. We assume there are $|V| = p$ number of nodes and $|W| = q = p(p - 1)/2$ number of edges. A binary graph $G_\epsilon = (V, W_\epsilon)$ of G is a graph with binary edge weight $w_{ij,\epsilon}$:

$$w_{ij,\epsilon} = \begin{cases} 1, & \text{if } w_{ij} > \epsilon, \\ 0, & \text{otherwise.} \end{cases}$$

A graph filtration of G is defined as a collection of nested binary networks:

$$G_{\epsilon_0} \supset G_{\epsilon_1} \supset \cdots \supset G_{\epsilon_k},$$

where $\epsilon_0 < \epsilon_1 < \cdots < \epsilon_k$ are filtration values [3, 22, 61].

By arranging the edge weights in increasing order,

$$w_{(1)} = \min_{j,k} w_{jk} < w_{(2)} < \cdots < w_{(q)} = \max_{j,k} w_{jk}, \quad (1)$$

where the subscript (\cdot) denotes the order statistic, we construct the graph filtration at these edge weights [22, 61]:

$$G_{w_{(1)}} \supset G_{w_{(2)}} \supset \cdots \supset G_{w_{(q)}}. \quad (2)$$

The graph filtration of a graph with 4 nodes is illustrated in Figure 1. Unlike the Vietoris-Rips filtration [16, 82], the graph filtration does not produce more than 1-dimensional homology. In a binary network G_ϵ , which is a simplicial complex consisting of only nodes and edges, 0-dimensional (0D) holes are *connected components* and 1-dimensional (1D) holes are *cycles*. The number of connected components and the number of independent cycles in a graph are referred to as the 0th Betti number (β_0) and 1st Betti number (β_1),

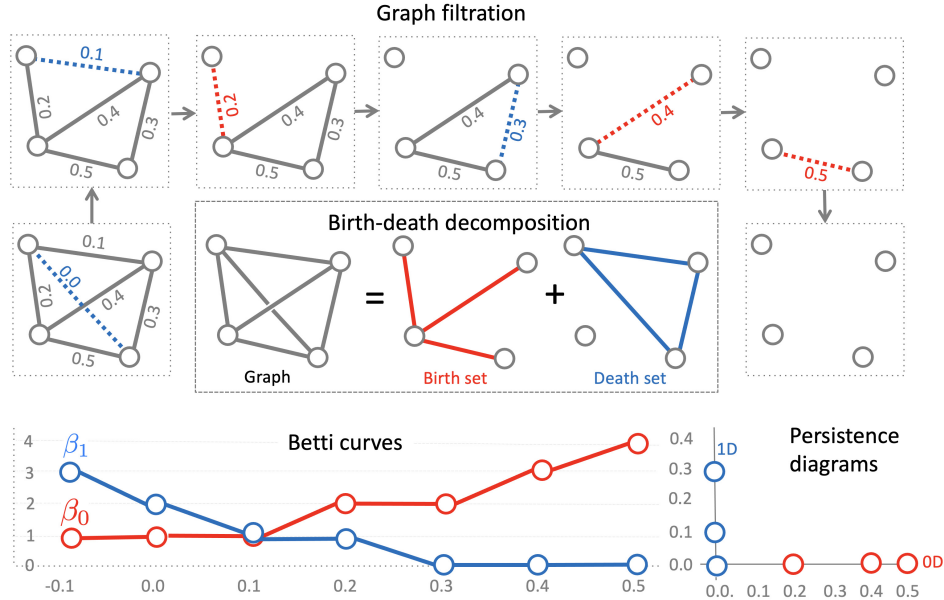


FIGURE 1. Graph filtration and the corresponding birth-death decomposition of a graph with 4 nodes. The birth-death decomposition partitions the edge set into disjoint birth and death sets. The resulting Betti curves are monotonic while the persistence diagrams are 1-dimensional points in \mathbb{R} .

respectively. In a graph filtration, the sequential removal of edges leads to either the birth of a connected component or the death of a cycle [22]. Once a connected component is born, it never dies. Therefore its death values are assumed to be at ∞ and ignored. On the other hand, all cycles are considered to be born at $-\infty$ and their birth values are ignored. Thus we can partition edge weights into the birth set $B(G)$ and death set $D(G)$. The birth set $B(G)$ consists of the sequence of increasing birth values

$$B(G) : b_1 < b_2 < \dots < b_{m_0},$$

where $m_0 = p - 1$ [61]. Ignoring the death values at ∞ , 0-dimensional persistent diagram is simply characterized by the birth set $B(G)$ (Figure 1). Further, the persistence diagram is also equivalent to the barcode. The death set $D(G)$ consists of the sequence of increasing death values

$$D(G) : d_1 < d_2 \dots < d_{m_1}.$$

During the graph filtration, the removal of an edge splits the graph into at most two components. Therefore, the number of connected components β_0 increases, and the increase is at most one [22]. The Euler characteristic χ of the graph is given by [1],

$$\chi = p - q = \beta_0 - \beta_1.$$

Thus,

$$\beta_1 = \beta_0 - p + q.$$

Note that p is fixed over the filtration, but q decreases by one while β_0 increases by at most one. Hence, β_1 always decreases, and the decrease is at most one [22]. The monotonic

properties of Betti numbers over filtration is illustrated in Figure 1. The total number of death values for a complete graph with p nodes was derived in [61] to be

$$m_1 = \beta_1 = 1 - p + \frac{p(p-1)}{2} = \frac{(p-1)(p-2)}{2}.$$

Ignoring the birth values at $-\infty$, 1-dimensional persistent diagram is characterized by the death set $B(G)$ (Figure 1). This also diverges from the Vietoris-Rips filtration, which produces cloud points in \mathbb{R}^2 as the 1-dimensional persistent diagram [6, 12, 19, 28]. Every edge of a graph must belong to either the birth set or the death set. This leads to the *birth-death decomposition* of a graph, which partitions the set of edge weights into the birth and death sets [61] as follows

$$W = B(G) \cup D(G), \quad B(G) \cap D(G) = \emptyset.$$

The birth-death decomposition of a graph is illustrated in Figure 1.

2.2. Wasserstein distance. The topological similarity or dissimilarity between two networks can be quantified using the *Wasserstein distance* between persistent diagrams [47, 48, 73, 62]. Let $G_1 = (V, W_1)$ and $G_2 = (V, W_2)$ be two given networks, each with p nodes. Let P_1 and P_2 be the corresponding persistent diagrams. The r -Wasserstein distance between P_1 and P_2 is then given by

$$\mathfrak{L}_r(P_1, P_2) = \inf_{\tau: P_1 \rightarrow P_2} \left(\sum_{x \in P_1} \|x - \tau(x)\|^r \right)^{1/r},$$

where the infimum is taken over every possible permutation or bijection τ between P_1 and P_2 [7, 52]. As r approaches infinity, the ∞ -Wasserstein distance is given by:

$$\mathfrak{L}_\infty(P_1, P_2) = \inf_{\tau: P_1 \rightarrow P_2} \max_{x \in P_1} \|x - \tau(x)\|$$

This distance is also known as the *Bottleneck distance* [24].

Standard methods for computing the Wasserstein distance, such as the Kuhn-Munkres and Hungarian algorithms, typically have a computational complexity of $\mathcal{O}(p^3)$ [30, 49, 61, 65, 66]. In contrast, for graph filtrations that yield 1-dimensional scatter plots as persistence diagrams, the Wasserstein distances can be calculated more efficiently with a computational complexity of $\mathcal{O}(p \log p)$ by directly matching sorted birth and death values.

Theorem 2.1. *For persistent diagrams P_1 and P_2 from graph filtrations, we have*

$$\mathfrak{L}_r(P_1, P_2) = \inf_{\tau: P_1 \rightarrow P_2} \left(\sum_{x \in P_1} |x - \tau(x)|^r \right)^{1/r} = \left(\sum_{x \in P_1} |x - \tau^*(x)|^r \right)^{1/r},$$

where τ^* maps the i -th smallest value in P_1 to the i -th smallest value in P_2 for all i . For $r \rightarrow \infty$,

$$\mathfrak{L}_\infty(P_1, P_2) = \inf_{\tau: P_1 \rightarrow P_2} \max_{x \in P_1} |x - \tau(x)| = \max_{x \in P_1} |x - \tau^*(x)|.$$

Proof. We prove for 0-dimensional persistence diagrams only; the proof for 1-dimensional diagrams is analogous. Suppose P_1 and P_2 consist of birth values

$$P_1 : b_1^1 < b_2^1 < \dots < b_{m_0}^1, \quad P_2 : b_1^2 < b_2^2 < \dots < b_{m_0}^2$$

respectively. Note τ^* is the identity permutation, i.e., $\tau^*(i) = i$. We aim to prove that

$$\sum_{i=1}^{m_0} |b_i^1 - b_i^2|^r \leq \sum_{i=1}^{m_0} |b_i^1 - b_{\tau(i)}^2|^r$$

for any permutation τ that is not the identity.

Consider a non-identity permutation τ . τ will include at least one pair $(i, \tau(i))$ where $i \neq \tau(i)$. Without loss of generality, assume $i < \tau(i)$. Then, $b_i^1 < b_{\tau(i)}^1$ and $b_i^2 < b_{\tau(i)}^2$. Hence,

$$b_i^1 - b_i^2 < b_{\tau(i)}^1 - b_i^2, \quad b_i^1 - b_{\tau(i)}^2 < b_{\tau(i)}^1 - b_i^2.$$

Subsequently,

$$|b_i^1 - b_i^2|^r + |b_{\tau(i)}^1 - b_{\tau(i)}^2|^r < |b_i^1 - b_{\tau(i)}^2|^r + |b_{\tau(i)}^1 - b_i^2|^r,$$

Summing over all such pairs $(i, \tau(i))$ shows that

$$\sum_{i=1}^{m_0} |b_i^1 - b_i^2|^r < \sum_{i=1}^{m_0} |b_i^1 - b_{\tau(i)}^2|^r,$$

thus proving the first statement. The second statement follows as

$$\mathfrak{L}_\infty(P_1, P_2) = \lim_{r \rightarrow \infty} \mathfrak{L}_r(P_1, P_2) = \lim_{r \rightarrow \infty} \left(\sum_{x \in P_1} |x - \tau^*(x)|^r \right)^{1/r} = \max_{x \in P_1} |x - \tau^*(x)|.$$

■

The theorem is related to the majorization theorem [46, 72]. Given ordered vectors $\alpha = (\alpha_1, \dots, \alpha_n)$ and $\beta = (\beta_1, \dots, \beta_n)$ satisfying

$$\alpha_1 \geq \alpha_2 \geq \dots \geq \alpha_n, \quad \beta_1 \geq \beta_2 \geq \dots \geq \beta_n,$$

α majorizes β if

$$\sum_{i=1}^k \alpha_i \geq \sum_{i=1}^k \beta_i, \quad \sum_{i=1}^n \alpha_i = \sum_{i=1}^n \beta_i.$$

for all $1 \leq k \leq n$. For α majorizing β and for any convex function f , we have [46, 72]

$$\sum_{i=1}^n f(\alpha_i) > \sum_{i=1}^n f(\beta_i).$$

Then by identifying α_i as the i -th largest element in the set $\{|x - \tau(x)| : x \in P_1\}$, β_i as the i -th largest element in the set $\{|x - \tau^*(x)| : x \in P_1\}$, and convex function $f(x) = |x|^r$, we obtain the desired result.

Theorem 2.2. *The Wasserstein distance satisfies the following inequality*

$$\mathfrak{L}_\infty(P_1, P_2) \leq \mathfrak{L}_p(P_1, P_2) \leq \mathfrak{L}_r(P_1, P_2) \leq \mathfrak{L}_1(P_1, P_2),$$

for $r < p < \infty$.

Proof. We will restrict our proof to 0-dimensional persistence diagrams; the proof for 1-dimensional diagrams follows analogously. Let P_1 and P_2 consist of birth values

$$P_1 : b_1^1 < b_2^1 < \dots < b_{m_0}^1, \quad P_2 : b_1^2 < b_2^2 < \dots < b_{m_0}^2$$

respectively. The r -Wasserstein distance between connected components is given by

$$\mathfrak{L}_r(P_1, P_2) = \sum_{i=1}^{m_0} (b_i^1 - b_i^2)^2 = \mathbf{b}_1^\top \mathbf{b}_2,$$

with the sorted vector $\mathbf{b}_k = (b_1^k, b_2^k, \dots, b_{m_0}^k)^\top$. Note \mathbf{b}_k is a point in the $(m_0 - 1)$ -simplex \mathcal{T}_0 defined as

$$\mathcal{T}_0 = \{(x_1, x_2, \dots, x_{m_0}) | x_1 < x_2 < \dots < x_{m_0}\} \subset \mathbb{R}^{m_0}$$

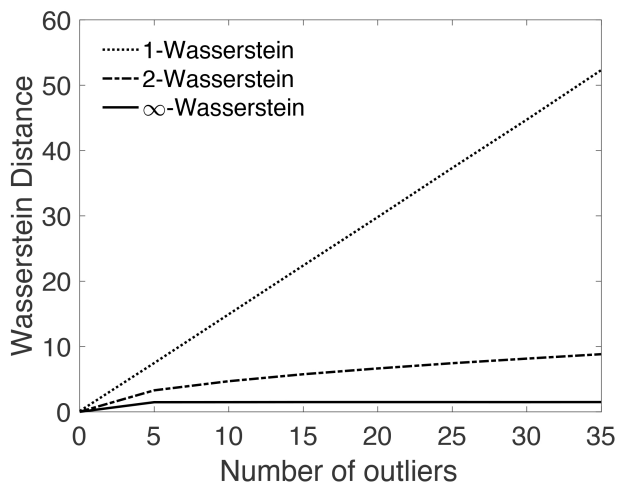


FIGURE 2. Comparison of 1-, 2-, and ∞ -Wasserstein distances as the number of outliers varies. The dataset consists of two sets of edge weight vectors of length 100, generated from $N(0, 0.01^2)$. Outliers were introduced into one set by replacing entries with values from $N(1.5, 0.01^2)$. The 1-Wasserstein distance is the upper bound of all other r -Wasserstein distances and it is severely impacted by the presence of outliers.

with x_1 bounded below and x_{m_0} bounded above. Hence, the 0D Wasserstein distance is equivalent to the Euclidean distance in the m_0 -dimensional convex set \mathcal{T}_0 . Thus, the Wasserstein distances satisfy the l_r -norm inequality for Euclidean distances in a convex set [10]. \blacksquare

Since the 1-Wasserstein distance sets the upper bound, it is generally not the most effective metric, especially when the data contains outliers. This is illustrated through a simulation study, where two sets of edge weight vectors of length 100 were generated from a normal distribution $N(0, 0.01^2)$ (Figure 2). Outliers were introduced into one of the edge weight vectors by replacing some entries with values generated from $N(1.5, 0.01^2)$. We computed the 1-, 2-, and ∞ -Wasserstein distances between the two sets and plotted the resulting distances in Figure 2. The distance should be close to zero when no outliers are present. However, our observations indicate that the 1-Wasserstein distance is severely impacted by the presence of outliers, showing a substantial inflation in value. On the other hand, the 2- and ∞ -Wasserstein distances are significantly more robust against such anomalies. Even when up to 35% of the data consists of outliers, the ∞ -Wasserstein distance provides reasonable results, while the 1-Wasserstein distance is not advisable for most applications.

2.3. Dynamic Embedding. Dynamically changing functional brain imaging data can be modeled as a d -variate time series, where d is the number of brain regions under investigation. A conventional technique for transforming univariate time series data into graph-based representations employs *time-delay embedding* (TDE), which is grounded in Takens' theorem [57]. Initially, TDE was aimed at uncovering the underlying dynamics of time series [67]. Recently, it has been used to analyze human speech [11] and to classify time series data [53, 31]. In TDE, each of the d univariate time series is transformed *individually*

using a sliding window of size M . This produces d distinct point clouds in \mathbb{R}^M (Figure 3). However, generalizing TDE to handle multivariate time series, such as those encountered in functional brain imaging data, is not straightforward. Moreover, TDE requires an additional step to estimate the dimension M from the data [60]. An incorrect estimation of M can lead to either overfitting or underfitting. Overfitting occurs when M is too large, where noise in the data is mistaken as though it was a feature. Underfitting takes place when M is too small to fully capture the dynamics. Motivated by TDE, we propose a new *Dynamic Embedding* that transforms a d -variate time series \mathbf{x}_t into a time-varying sequence of point clouds in \mathbb{R}^d .

Let $\mathbf{x}_t = (x_{1t}, \dots, x_{dt})^\top$ be a d -variate time series. At each time t , we project \mathbf{x}_t as a point in \mathbb{R}^d , where x_{it} serves as the i -th coordinate of the point. A sliding window $[t, t + p - 1]$ covering the time series $\mathbf{x}_t, \dots, \mathbf{x}_{t+p-1}$ yields p points in \mathbb{R}^d (Figure 3). The Euclidean distance between these points will be used as edge weights for building time-varying graph $G_t = (V_t, W_t)$, where the vertex set $V_t = \{\mathbf{x}_t, \dots, \mathbf{x}_{t+p-1}\}$ and the edge weights W_t are the Euclidean distances between corresponding points. Subsequently, we construct graph filtrations to obtain dynamically changing 0-dimensional and 1-dimensional persistent diagrams, represented as time varying birth and death values

$$B(G_t) = \{b_{1t}, \dots, b_{m_0t}\}, \quad D(G_t) = \{d_{1t}, \dots, d_{m_1t}\}$$

respectively. Unlike TDE, which implicitly incorporates the dynamic features of the time series into a point cloud, Dynamic Embedding has the distinct advantage of easily extracting the dynamic topological characteristics of the time series.

Figure 3 illustrates the difference between TDE and Dynamic Embedding. A univariate time series is constructed as

$$x_t = \sin(4\pi t), \quad t = 0, 1, 2, \dots, 100,$$

and used in TDE with window sizes $M = 3, 5$. For the window size $M = 3$, TDE produces a static point cloud in \mathbb{R}^3 . The coordinates are color-coded: red for the x -coordinate, green for the y -coordinate, and blue for the z -coordinate. TDE reveals a cyclic pattern due to the periodicity of the time series. A trivariate time series is constructed as

$$\mathbf{x}_t = (\sin(4\pi t), \cos(4\pi t), \sin(8\pi t))^\top, \quad t = 0, 1, 2, \dots, 100.$$

Dynamic Embedding is applied to produce a dynamically changing point cloud in \mathbb{R}^3 . Due to the periodicity, it warps around to form a closed loop. The coordinates are color-coded as red (x -coordinate), green (y -coordinate), and blue (z -coordinate), each corresponding to one of the time series. The Dynamic Embedding also reveals the cyclic pattern resulting from the periodicity of the time series.

Consider two d -variate time series $\mathbf{x}_t = (x_{1t}, \dots, x_{dt})^\top$ and $\mathbf{y}_t = (y_{1t}, \dots, y_{dt})^\top$ [42, 58, 33, 9]. We aim to determine the topological differences between these time series. Following Dynamic Embedding, we construct time-varying graphs X_t and Y_t with p nodes corresponding to the time series \mathbf{x}_t and \mathbf{y}_t , respectively. The total number of birth values of connected components and the total number of death values of cycles are given by [61]

$$m_0 = p - 1, \quad m_1 = 1 + \frac{p(p - 3)}{2}.$$

We can compute the 0-dimensional and 1-dimensional persistence diagrams at time t corresponding to the time series \mathbf{x}_t and \mathbf{y}_t . The r -Wasserstein distance between the 0-dimensional persistence diagrams at time t is given by

$$\mathfrak{L}_r^b(\mathbf{x}_t, \mathbf{y}_t) = \left(\sum_{k=1}^{m_0} |b_{kt}^{\mathbf{x}} - b_{kt}^{\mathbf{y}}|^r \right)^{1/r},$$

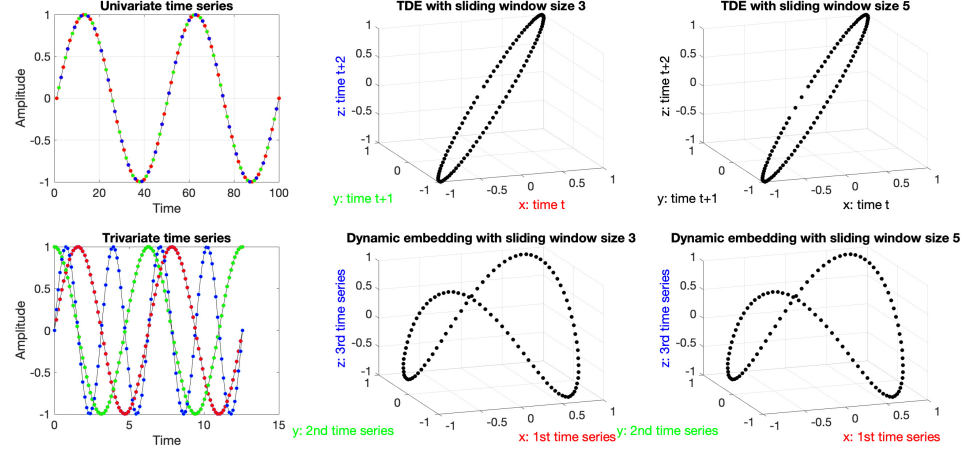


FIGURE 3. Top: time delay embedding (TDE) of a univariate time series. Sliding windows of sizes 3 and 5 are used to embed the time series as a static point cloud in \mathbb{R}^3 and \mathbb{R}^5 , respectively. In the case of a sliding window of size 3, the times 1, 4, 7, … provide the x -coordinates (red), 2, 5, 8, … provide the y -coordinates (green), and 3, 6, 9, … provide the z -coordinates (blue). In TDE, the window size determines the embedding dimension. Bottom: The proposed Dynamic Embedding of a trivariate time series. Sliding windows of sizes 3 and 5 are used to embed the time series into dynamically changing point clouds in \mathbb{R}^3 . However, due to the periodicity of the trivariate time series, the dynamically changing point clouds forms a closed loop. Unlike TDE, where the window size determines the embedding dimension, in Dynamic Embedding, it is the number of time series variables that determines the embedding dimension. Both embedding techniques are capable of capturing the underlying circular topology over time.

where b_{kt}^x and b_{kt}^y are the k -th smallest birth values associated with the graphs X_t and Y_t , respectively. Similarly, the r -Wasserstein distance between the 1-dimensional persistence diagrams at time t is

$$\mathcal{L}_r^d(\mathbf{x}_t, \mathbf{y}_t) = \left(\sum_{k=1}^{m_1} |d_{kt}^x - d_{kt}^y|^r \right)^{1/r},$$

where d_{kt}^x and d_{kt}^y are the k -th smallest death values associated with the graphs X_t and Y_t , respectively. Lastly, the ∞ -Wasserstein distances are given by

$$\mathcal{L}_\infty^b(\mathbf{x}_t, \mathbf{y}_t) = \max_{1 \leq k \leq m_0} |b_{kt}^x - b_{kt}^y|$$

and

$$\mathcal{L}_\infty^d(\mathbf{x}_t, \mathbf{y}_t) = \max_{1 \leq k \leq m_1} |d_{kt}^x - d_{kt}^y|.$$

Subsequently, we propose to combine the r -Wasserstein distances over all time as

$$\mathcal{L}_r(\mathbf{x}_t, \mathbf{y}_t) = \sum_t \mathcal{L}_r^b(\mathbf{x}_t, \mathbf{y}_t) + \sum_t \mathcal{L}_r^d(\mathbf{x}_t, \mathbf{y}_t).$$

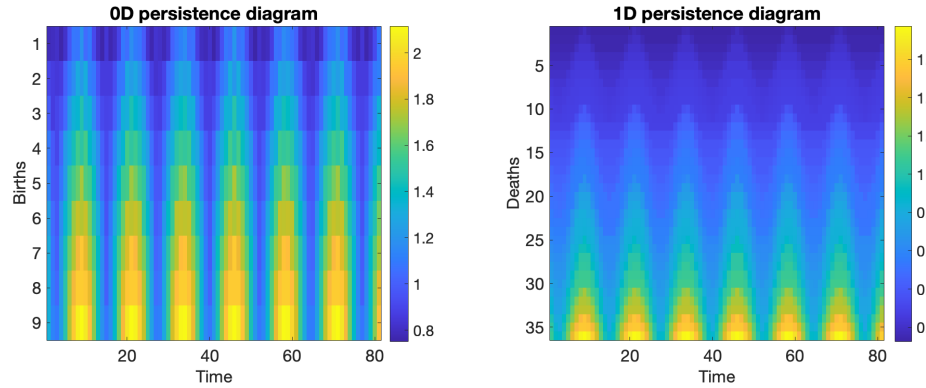


FIGURE 4. The time-varying persistence diagrams for the Dynamic Embedding on the trivariate time series in Figure 3-bottom with a sliding window size of 10. The embedding yields 9 dynamically changing cloud points per window. The persistence diagrams generated from the graph filtration yield sorted birth (0-dimensional) and death (1-dimensional) values. If a smaller window size, such as 3, is used, it produces only 2 points, rendering the topology too crude for accurate estimation. A larger window size was selected to provide sufficient points for a more accurate estimation of the underlying topology. The periodic pattern observed in the persistence diagrams is a consequence of the periodicity present in the trivariate time series.

For $r \rightarrow \infty$, we have

$$\mathcal{L}_\infty(\mathbf{x}_t, \mathbf{y}_t) = \sum_t \mathcal{L}_\infty^b(\mathbf{x}_t, \mathbf{y}_t) + \sum_t \mathcal{L}_\infty^d(\mathbf{x}_t, \mathbf{y}_t).$$

A large value of $\mathcal{L}_r(\mathbf{x}, \mathbf{y})$ or $\mathcal{L}_\infty(\mathbf{x}, \mathbf{y})$ suggests that the dynamic persistence diagrams generated from the two time series \mathbf{x}_t and \mathbf{y}_t are *topologically distant*. This indicates a significant difference in the 0-dimensional and 1-dimensional topological features between \mathbf{x}_t and \mathbf{y}_t . Since the distributions of the proposed test statisticss $\mathcal{L}_r(\mathbf{x}_t, \mathbf{y}_t)$ and $\mathcal{L}_\infty(\mathbf{x}_t, \mathbf{y}_t)$ are unknown, we employ the permutation test for inference. The permutation test does not make any assumptions about the underlying probability distribution [23, 68, 81, 50, 80].

2.4. Topological inference on Dynamic Embedding. Suppose we have m and n d -variate time series in two groups. Given two sets of d -variate time series, $\{\mathbf{x}^1, \mathbf{x}^2, \dots, \mathbf{x}^m\}$ and $\{\mathbf{y}^1, \mathbf{y}^2, \dots, \mathbf{y}^n\}$, we aim to compute the p -value to test the null hypothesis that the two sets of time series are topologically equivalent. The topological similarity is measured through the Wasserstein distance. For each pair of time series \mathbf{x}^i and \mathbf{y}^j , we compute the Wasserstein distance $\mathcal{L}_r(\mathbf{x}^i, \mathbf{y}^j)$ using birth and death values obtained from topological features.

We consider the combined ordered set

$$\mathbf{z} = \{\mathbf{z}^1, \dots, \mathbf{z}^{m+n}\} = \{\mathbf{x}^1, \mathbf{x}^2, \dots, \mathbf{x}^m, \mathbf{y}^1, \mathbf{y}^2, \dots, \mathbf{y}^n\}.$$

The between-group distance $d(\mathbf{z})$ is given by the total sum of pairwise Wasserstein distances:

$$d(\mathbf{z}) = \sum_{i=1}^m \sum_{j=1}^n \mathcal{L}_r(\mathbf{x}^i, \mathbf{y}^j).$$

This can be used as a test statistic. Since the distribution is unknown, the statistical significance can be determined through the scalable version of permutation test through transpositions [23, 61]. We first compute the pairwise distance matrix $D = (d_{ij}) = (\mathcal{L}_r(\mathbf{z}^i, \mathbf{z}^j))$. Once D is computed, there is no need to recompute it for each permutation. We only need to shuffle the entries of D by permutation as follows.

The between-group distance can be expressed as

$$d(\mathbf{z}) = \sum_{i=1}^m \sum_{j=m+1}^{m+n} d_{ij} = \mathbf{1}_m^\top D \mathbf{1}_n,$$

where $\mathbf{1}_m$ and $\mathbf{1}_n$ are indicator vectors of dimension $m + n$ for each group such that

$$\mathbf{1}_m = [1, \dots, 1, 0, \dots, 0]^\top, \quad \mathbf{1}_n = [0, \dots, 0, 1, \dots, 1]^\top.$$

There are m 1's in $\mathbf{1}_m$ and n 1's in $\mathbf{1}_n$. Let $\pi \in \mathbb{S}_{m+n}$ be a permutation for integers $\{1, \dots, m+n\}$ in the permutation group of order $m+n$. For permutation $\mathbf{z}^\pi = \{\mathbf{z}^{\pi(1)}, \dots, \mathbf{z}^{\pi(m+n)}\}$ which permutes entries of \mathbf{z} , the permuted between-group distance $d(\mathbf{z}^\pi)$ can be represented as

$$d(\mathbf{z}^\pi) = \mathbf{1}_m^\top \Pi D \Pi^\top \mathbf{1}_n, \quad (3)$$

with the permutation matrix $\Pi = (q_{ij})$ defined as a $(m+n) \times (m+n)$ matrix such that $q_{ij} = 1$ if $\pi(i) = j$ and $q_{ij} = 0$ otherwise. After the permutation, the Wasserstein distance incrementally changes to

$$d(\mathbf{z}^\pi) = d(\mathbf{z}) + \Delta d, \quad (4)$$

where $\Delta d = \mathbf{1}_m^\top (\Pi D \Pi^\top - \Pi) \mathbf{1}_n$ is the increment over permutation π . The computation of $d(\mathbf{z}^\pi)$ leverages term $d(\mathbf{z})$ recycled from the previous iteration. When only one entry from each group is permuted, we have transpositions, and the iterative update for Δd in equation (4) involves only a small number of terms and we can further increase the rate of convergence [23, 61]. Thus, in numerical implementations, we intersperse a full permutation after every 1000 transpositions.

Since $d(\mathbf{z})$ increases as the number of networks m and n increases, we normalized it as

$$\lambda(\mathbf{z}) = \frac{d(\mathbf{z})}{\sum_{i=1}^{m+n} \sum_{j=1}^{m+n} \mathcal{L}_r(\mathbf{z}^i, \mathbf{z}^j) - d(\mathbf{z})}.$$

The sum of all pairwise distances $\sum_{i=1}^{m+n} \sum_{j=1}^{m+n} \mathcal{L}_r$ is fixed regardless of how we assign group labels. The denominator is the within-group distance, which is the sum of all pairwise distance within each group. Subsequently, we use the ratio $\lambda(\mathbf{z})$ as a test statistic for testing the equality of two sets of d -variate time series. The p -value is then calculated as the proportion of permutations where $\lambda(\mathbf{z}^\pi)$ exceeds $\lambda(\mathbf{z})$:

$$p\text{-value} = \frac{1}{(m+n)!} \sum_{\pi \in \mathbb{S}_{m+n}} \mathcal{I}(\lambda(\mathbf{z}^\pi) > \lambda(\mathbf{z})), \quad (5)$$

where \mathcal{I} is an indicator variable taking value 1 if the argument is true and 0 otherwise [23]. Since the computation for every possible permutation is too time consuming, we usually perform uniform sampling in \mathbb{S}_{m+n} . Once incremental formula (4) is identified, the p -value can be computed iteratively over permutations. At the k -th permutation, the p -value p_k is updated as

$$(k+1)p_{k+1} = kp_k + \mathcal{I}(\lambda(\mathbf{z}^\pi) > \lambda(\mathbf{z})). \quad (6)$$

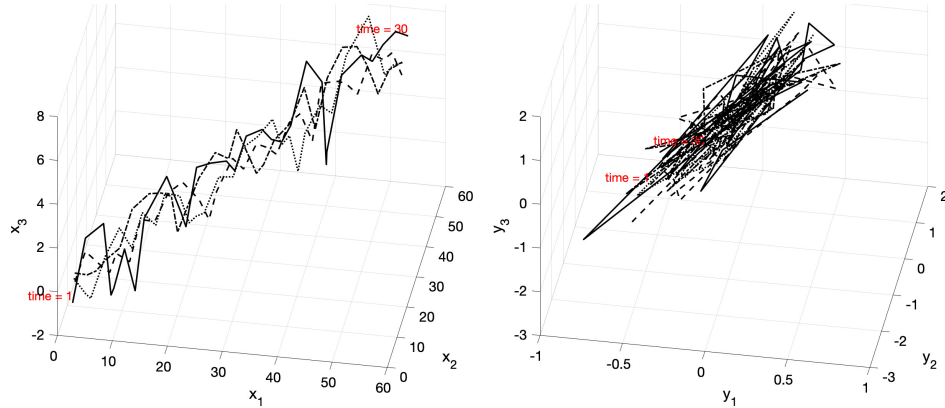


FIGURE 5. Four independently simulated trivariate time series $\mathbf{x}_t = (x_1(t), x_2(t), x_3(t))^\top$ (equation 7) and $\mathbf{y}_t = (y_1(t), y_2(t), y_3(t))^\top$ (equation 8) in Study 1. Each trivariate time series is represented as a random walk of length 30 in \mathbb{R}^3 . The Wasserstein distance was able to discriminate between samples generated from \mathbf{x}_t and \mathbf{y}_t , but did not detect any differences in samples generated solely from \mathbf{x}_t .

The MATLAB code for Dynamic Embedding and topological inference are available at <https://github.com/laplcebeltrami/PH-STAT>.

3. Simulation Studies. Since there is no ground truth in real data, we performed two simulation studies with specified ground truths for testing false-negatives and false-positives. These controlled experiments were utilized to assess the performance of the proposed method. Consider a trivariate time series generated by a vector autoregressive model of order one [83, 45, 38]:

$$\mathbf{x}_t = \mathbf{a} + \mathbf{b}t + \Theta \mathbf{x}_{t-1} + \xi_t, \quad (7)$$

with noise $\xi_t \sim N(0, \Sigma)$ at time t (Figure 5). We also considered a different trivariate time series consisting solely of Gaussian white noise at time t :

$$\mathbf{y}_t \sim N(0, \Sigma). \quad (8)$$

The trend parameters were set to $\mathbf{a} = (1, 1, 0)^\top$ and $\mathbf{b} = (1.5, 2, 0)^\top$ for $1 \leq t \leq 30$. The coefficient and covariance matrices are chosen as

$$\Theta = \begin{bmatrix} 0.2 & -0.1 & 0.5 \\ -0.4 & 0.2 & 0 \\ -0.1 & 0.2 & 0.3 \end{bmatrix}, \quad \Sigma = \begin{bmatrix} 0.1 & 0.01 & 0.3 \\ 0.01 & 0.5 & 0 \\ 0.3 & 0 & 1 \end{bmatrix}.$$

For simulations, we generated 10 time series for each time series $\mathbf{x}_t, \mathbf{y}_t$ and \mathbf{z}_t . Used $p = 10$ as size of sliding window for Dynamic Embedding. The transposition test with 100,000 transpositions were used to determine statistical significance.

3.1. When there is difference in time series. We tested if the method can detect topological differences in time series \mathbf{x}_t and \mathbf{y}_t (Figure 5). We used $\mathcal{L}_2(\mathbf{x}_t, \mathbf{y}_t)$ as the test statistic. Each simulation is independently replicated 10 times, and the resulting p -values are averaged. The computed p -values are $(0.50 \pm 0.97) \times 10^{-5}$, signifying a robust topological disparity between the two trivariate time series.

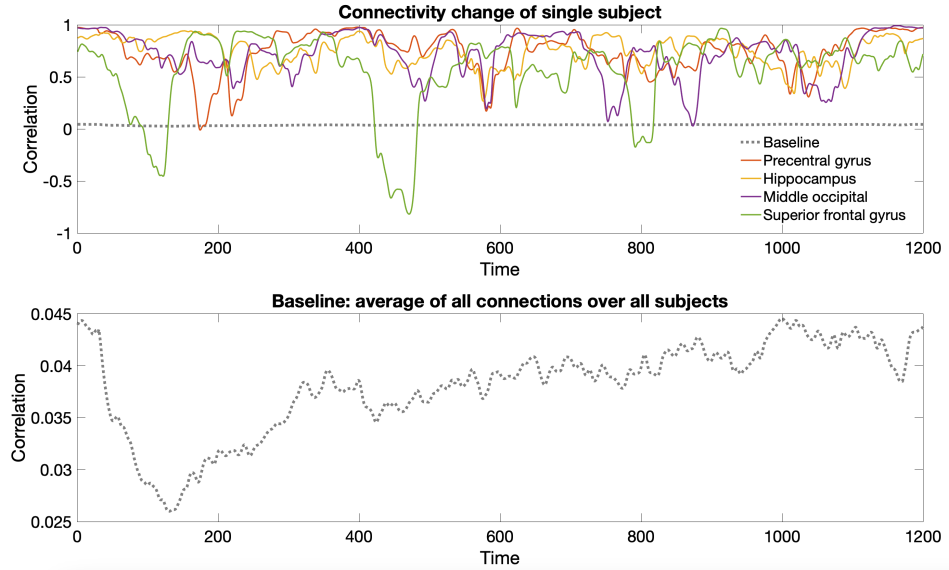


FIGURE 6. Top: Time series of functional brain connectivity between the left and right hemispheres across 4 regions. We analyzed a total of 6670 time series of brain connectivity between 116 regions in this study. Bottom: The average time series of functional brain connectivity, averaged over all connections and subjects. We removed the first 60 time points in the subsequent analysis. Although a slight increasing trend is observed, it is negligible when compared to the individual connectivities.

3.2. When there is no difference in time series. To assess the false-positive rate of our method, we introduce another time series z_t , which is modeled identically to x_t but with independently generated noise (Figure 5). In this case, we do not expect our method to identify any topological differences between x_t and z_t . The simulation was conducted 10 times independently, and the results were averaged. The computed p -values are 0.33 ± 0.20 , confirming that our method does not incorrectly identify topological differences.

4. Application to functional brain images.

4.1. Data description. We used a resting-state fMRI dataset collected as part of the Human Connectome Project (HCP) [75, 36]. The dataset consists of fMRI scans of 412 subjects (172 males and 240 females) measured over 1200 time points using a gradient-echoplanar imaging sequence [61, 3]. Since there are more than 300000 voxels in an fMRI scan, we parcellated the brain into 116 non-overlapping anatomical regions using the Automated Anatomical Labeling (AAL) template and averaged rsfMRI over each parcellation [69, 26, 37, 4]. The head movements cause serious spatial artifacts in functional connectivity [54, 74, 55, 15]. We calculated the framewise displacements from the three translational displacements and three rotational displacements at each time point to measure the head movement from one volume to the next. The volumes with framewise displacement larger than 0.5 mm from their neighbors (one back and two forward time points) were scrubbed [74, 54, 40]. More than one third of 1200 volumes were scrubbed in 12 subjects. Thus, we removed the 12 subjects (4 males and 8 females) and used 400 subjects for the study. Following [2], we adopted window size 60 repetition time (TR), which is time taken for the

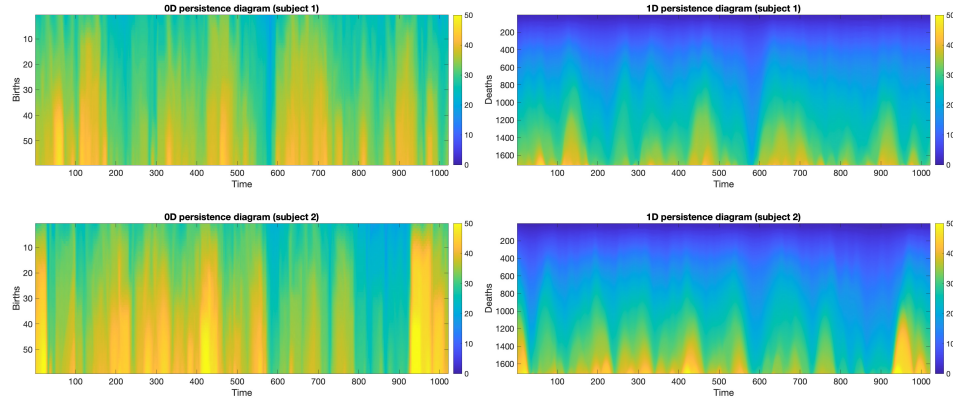


FIGURE 7. Dynamically changing persistence diagrams for subject 1 (top) and subject 2 (bottom). The persistence diagrams were computed on time varying graphs obtained through Dynamic Embedding in \mathbb{R}^{60} . We employed the 2-Wasserstein distance to measure topological similarity between the subjects within a window of 60 TRs, equivalent to 43.2 seconds.

MRI sequence to acquire one whole volume. Since TR=0.72 seconds in HCP, it is 43.2 seconds in physical time. Subsequently we computed the Pearson correlation between brain regions in each sliding window in measuring the strength of time varying brain connectivity. The details on the rsfMRI preprocessing we performed is explained in our previous study [40]. There are total $(116 \times 115)/2 = 6670$ time series of brain connectivity between 116 regions per subject that is used as an input to this study.

The time series are averaged over all connections to determine if there is an overall trend (Figure 6-bottom). We observe a sharp decline in the initial measurements of fMRI, which is usually considered as artifacts included by the large variance at the beginning of each MRI scan [40, 27]. Thus, we removed the first 60 time points and only used the remaining 1140 time points in the subsequent analysis. There exists a slow increasing trend (Figure 6-bottom). However, the trend is negligible when compared to the individual connectivities. Further, the time-varying graph G_t obtained in the Dynamic Embedding is invariant of changes in the baseline fMRI signal. If there's a general upward or downward trend in the fMRI data over time, this will not have an impact on the structure of graph G_t . Therefore, we applied our method directly to the fMRI connectivity without the need for detrending.

4.2. Global topological inference. We applied our method to determine if there is overall topological difference between resting-state functional brain connectivity between males and females. Sex differences in rs-fMRI have been a subject of considerable research interest. Studies have found that males and females exhibit different patterns of functional connectivity in the default mode network [8]. Research on specific brain regions like the amygdala has shown sex-specific connectivity patterns that could be linked to emotional processing [43]. Sex differences in the rs-fMRI connectivity of the brain could be related to cognitive performance and behavioral traits [56]. In diffusion tensor imaging study, males have been observed to have greater within-hemisphere connectivity, whereas females have greater between-hemisphere connectivity [41].

We performed Dynamic Embedding on $d = 6670$ time-varying connectivities. We employed a sliding window approach with a window size of $p = 60$. This window size was

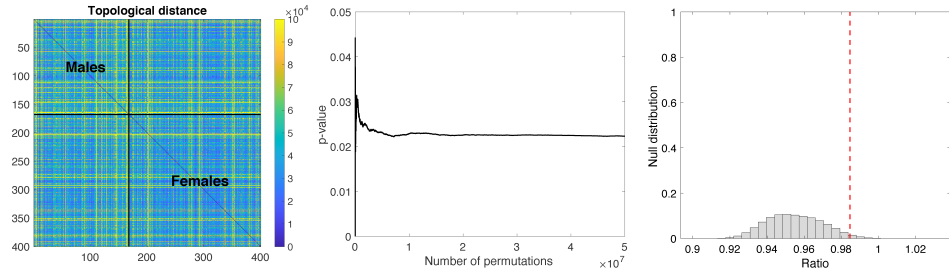


FIGURE 8. Left: Distance matrix $\mathcal{L}_2(\mathbf{z}^i, \mathbf{z}^j)$. Males have slightly larger topological distance compared to females. Middle: plot showing the convergence of p -value over increasing permutations. At 50 million permutations, the estimated p -value is stable. Right: the empirical null distribution obtained from 50 million permutations. The red line is the observed ratio statistic of the between-group over within-group distances.

chosen to match the sliding window used for computing correlations to ensure consistency across different analytical methods and to minimize aliasing artifacts. Aliasing occurs when a signal is sampled at a rate leading to distortions or inaccuracies in the reconstructed signal. By aligning the window sizes, we enhanced the robustness and interpretability of our results. Figure 7 displays the time-varying persistence diagrams for two subjects. There are total $m = 168$ males and $n = 232$ females. We performed the permutation test with 50 million random transpositions intermixed with one full permutation every 1000 transpositions on the Wasserstein distance \mathcal{L}_2 in discriminating sex. We obtain the observed ratio statistic of 0.9846 and the corresponding p -value 0.0223. Thus, we conclude that the proposed method distinctly discriminates the functional connectivity between females and males. Figure 8 plots the histogram of the test statistic and the corresponding observed test statistic (in dashed red).

5. Conclusion. Topological data analysis (TDA) based approaches have been previously applied to static brain imaging studies [21, 5, 77], focusing on identifying topological features that characterize brain signals. However, these methods are primarily tailored for investigating static summaries of brain networks, which inherently limits their ability to provide comprehensive insights. In this paper, we introduce a new framework for dynamic-TDA that is capable of statistically discriminating between two groups of multivariate time series. Our proposed methodology builds on persistent homology over multivariate time series and constructs a statistical measure based on r -Wasserstein distances between persistence diagrams. We have applied this approach to resting-state fMRI data from both female and male human subjects and discovered significant topological differences in terms of combined 0D and 1D topological distances between the two groups. Given the success of the proposed approach in differentiating multivariate time series, we believe that it can be extended to analyze other types of time series data as well.

Acknowledgments. This study is funded by NIH EB02875, MH133614, NSF MDS-2010778 and the King Abdullah University of Science and Technology (KAUST) CRG. The use of CHAT-GPT is acknowledged.

REFERENCES

- [1] R. Adler, O. Bobrowski, M. Borman, E. Subag and S. Weinberger, Persistent homology for random fields and complexes, in *Borrowing strength: theory powering applications—a Festschrift for Lawrence D. Brown*, Institute of Mathematical Statistics, 2010, 124–143.
- [2] E. Allen, E. Damaraju, S. Plis, E. Erhardt, T. Eichele and V. Calhoun, Tracking whole-brain connectivity dynamics in the resting state, *Cerebral cortex*, **24** (2014), 663–676.
- [3] D. Anand and M. Chung, Hodge-Laplacian of brain networks, *IEEE Transactions on Medical Imaging*, **42** (2023), 1563–1473.
- [4] S. Arslan, S. Ktena, A. Makropoulos, E. Robinson, D. Rueckert and S. Parisot, Human brain mapping: A systematic comparison of parcellation methods for the human cerebral cortex, *NeuroImage*, **170** (2018), 5–30.
- [5] D. Bassett and O. Sporns, Network neuroscience, *Nature neuroscience*, **20** (2017), 353–364.
- [6] E. Berry, Y.-C. Chen, J. Cisewski-Kehe and B. T. Fasy, Functional summaries of persistence diagrams, *Journal of Applied and Computational Topology*, **4** (2020), 211–262.
- [7] J. J. Berwald, J. M. Gottlieb and E. Munch, Computing Wasserstein distance for persistence diagrams on a quantum computer, *arXiv preprint arXiv:1809.06433*.
- [8] B. Biswal, M. Mennes, X.-N. Zuo, S. Gohel, C. Kelly, S. Smith, C. Beckmann, J. Adelstein, R. Buckner, S. Colcombe et al., Toward discovery science of human brain function, *Proceedings of the National Academy of Sciences*, **107** (2010), 4734–4739.
- [9] H. Böhm, H. Ombao, R. von Sachs and J. Sanes, Classification of multivariate non-stationary signals: The slex-shrinkage approach, *Journal of statistical planning and inference*, **140** (2010), 3754–3763.
- [10] S. Boyd and L. Vandenberghe, *Convex Optimization*, Cambridge University Press, 2004.
- [11] K. A. Brown and K. P. Knudson, Nonlinear statistics of human speech data, *International Journal of Bifurcation and Chaos*, **19** (2009), 2307–2319.
- [12] P. Bubenik, Statistical topological data analysis using persistence landscapes, *Journal of Machine Learning Research*, **16** (2015), 77–102.
- [13] P. Bubenik and P. Kim, A statistical approach to persistent homology, *Homology Homotopy and Applications*, **9** (2007), 337–362.
- [14] E. Bullmore and O. Sporns, Complex brain networks: graph theoretical analysis of structural and functional systems, *Nature Review Neuroscience*, **10** (2009), 186–98.
- [15] C. Caballero-Gaudes and R. Reynolds, Methods for cleaning the BOLD fMRI signal, *NeuroImage*, **154** (2017), 128–149.
- [16] E. Carlsson, J. G. Carlsson and S. Sweitzer, Applying topological data analysis to local search problems, *Foundations of Data Science*.
- [17] G. Carlsson, Topology and data, *Bulletin of the American Mathematical Society*, **46** (2009), 255–308.
- [18] G. Carlsson and F. Memoli, Persistent clustering and a theorem of J. Kleinberg, *arXiv preprint arXiv:0808.2241*.
- [19] F. Chazal, B. T. Fasy, F. Lecci, A. Rinaldo and L. Wasserman, Stochastic convergence of persistence landscapes and silhouettes, in *Proceedings of the thirtieth annual symposium on Computational geometry*, 2014, 474–483.
- [20] M. Chung, J. Hanson, H. Lee, N. Adluru, A. L. Alexander, R. Davidson and S. Pollak, Persistent homological sparse network approach to detecting white matter abnormality in maltreated children: MRI and DTI multimodal study, *MICCAI, Lecture Notes in Computer Science (LNCS)*, **8149** (2013), 300–307.
- [21] M. Chung, S.-G. Huang, A. Gritsenko, L. Shen and H. Lee, Statistical inference on the number of cycles in brain networks, in *2019 IEEE 16th International Symposium on Biomedical Imaging (ISBI 2019)*, IEEE, 2019, 113–116.
- [22] M. Chung, H. Lee, A. DiChristofano, H. Ombao and V. Solo, Exact topological inference of the resting-state brain networks in twins, *Network Neuroscience*, **3** (2019), 674–694.
- [23] M. Chung, L. Xie, S.-G. Huang, Y. Wang, J. Yan and L. Shen, Rapid acceleration of the permutation test via transpositions, *11848* (2019), 42–53.
- [24] D. Cohen-Steiner, H. Edelsbrunner and J. Harer, Stability of persistence diagrams, *Discrete & computational geometry*, **37** (2007), 103–120.
- [25] S. de Lange, M. de Reus and M. Van Den Heuvel, The laplacian spectrum of neural networks, *Frontiers in computational neuroscience*, **7** (2014), 189.
- [26] R. Desikan, F. Ségonne, B. Fischl, B. Quinn, B. Dickerson, D. Blacker, R. Buckner, A. Dale, R. Maguire, B. Hyman, S. Marilyn and J. Ronald, An automated labeling system for subdividing the human cerebral cortex on mri scans into gyral based regions of interest, *NeuroImage*, **31** (2006), 968–980.

- [27] J. Diedrichsen and R. Shadmehr, Detecting and adjusting for artifacts in fMRI time series data, *NeuroImage*, **27** (2005), 624–634.
- [28] H. Edelsbrunner and J. Harer, Persistent homology - a survey, *Contemporary Mathematics*, **453** (2008), 257–282.
- [29] H. Edelsbrunner, D. Letscher and A. Zomorodian, Topological persistence and simplification, in *Foundations of Computer Science, 2000. Proceedings. 41st Annual Symposium on*, IEEE, 2000, 454–463.
- [30] J. Edmonds and R. Karp, Theoretical improvements in algorithmic efficiency for network flow problems, *Journal of the ACM (JACM)*, **19** (1972), 248–264.
- [31] S. Emrani, T. Gentimis and H. Krim, Persistent homology of delay embeddings and its application to wheeze detection, *IEEE Signal Processing Letters*, **21** (2014), 459–463.
- [32] A. Fornito, A. Zalesky and E. Bullmore, *Fundamentals of Brain Network Analysis*, Academic Press, New York, 2016.
- [33] P. Fryzlewicz and H. Ombao, Consistent classification of nonstationary time series using stochastic wavelet representations, *Journal of the American Statistical Association*, **104** (2009), 299–312.
- [34] R. Ghrist, Barcodes: The persistent topology of data, *Bulletin of the American Mathematical Society*, **45** (2008), 61–75.
- [35] M. Gidea and Y. Katz, Topological data analysis of financial time series: Landscapes of crashes, *Physica A: Statistical Mechanics and its Applications*, **491** (2018), 820–834.
- [36] M. F. Glasser, S. N. Sotiroopoulos, J. A. Wilson, T. S. Coalson, B. Fischl, J. L. Andersson, J. Xu, S. Jbabdi, M. Webster, J. R. Polimeni et al., The minimal preprocessing pipelines for the Human Connectome Project, *Neuroimage*, **80** (2013), 105–124.
- [37] P. Hagmann, M. Kurant, X. Gigandet, P. Thiran, V. Wedeen, R. Meuli and J. Thiran, Mapping human whole-brain structural networks with diffusion MRI, *PLoS One*, **2** (2007), e597.
- [38] J. M. Haslbeck, L. F. Bringmann and L. J. Waldorp, A tutorial on estimating time-varying vector autoregressive models, *Multivariate Behavioral Research*, **56** (2021), 120–149.
- [39] C. Hu, L. Cheng, J. Sepulcre, K. A. Johnson, G. E. Fakhri, Y. M. Lu and Q. Li, A spectral graph regression model for learning brain connectivity of alzheimer’s disease, *PloS one*, **10** (2015), e0128136.
- [40] S.-G. Huang, S.-T. Samdin, C. Ting, H. Ombao and M. Chung, Statistical model for dynamically-changing correlation matrices with application to brain connectivity, *Journal of Neuroscience Methods*, **331** (2020), 108480.
- [41] M. Ingallhalikar, A. Smith, D. Parker, T. Satterthwaite, M. Elliott, K. Ruparel, H. Hakonarson, R. Gur, R. Gur and R. Verma, Sex differences in the structural connectome of the human brain, *Proceedings of the National Academy of Sciences*, **111** (2014), 823–828.
- [42] Y. Kakizawa, R. H. Shumway and M. Taniguchi, Discrimination and clustering for multivariate time series, *Journal of the American Statistical Association*, **93** (1998), 328–340.
- [43] L. Kilpatrick, D. Zald, J. Pardo and L. Cahill, Sex-related differences in amygdala functional connectivity during resting conditions, *NeuroImage*, **30** (2006), 452–461.
- [44] H. Lee, H. Kang, M. Chung, B.-N. Kim and D. Lee, Persistent brain network homology from the perspective of dendrogram, *IEEE Transactions on Medical Imaging*, **31** (2012), 2267–2277.
- [45] H. Lütkepohl, Vector autoregressive models, in *Handbook of Research Methods and Applications in Empirical Macroeconomics*, Edward Elgar Publishing, 2013, 139–164.
- [46] A. Marshall, I. Olkin and B. Arnold, Inequalities: theory of majorization and its applications.
- [47] L. Mi, W. Zhang, X. Gu and Y. Wang, Variational wasserstein clustering, in *Proceedings of the European Conference on Computer Vision (ECCV)*, 2018, 322–337.
- [48] L. Mi, W. Zhang and Y. Wang, Regularized wasserstein means for aligning distributional data, in *Proceedings of the AAAI Conference on Artificial Intelligence*, vol. 34, 2020, 5166–5173.
- [49] J. R. Munkres, Algorithms for the assignment and transportation problems, *Journal of the Society for Industrial and Applied Mathematics*, **5** (1957), 32–38.
- [50] T. Nichols and A. Holmes, Nonparametric permutation tests for functional neuroimaging: A primer with examples, *Human Brain Mapping*, **15** (2002), 1–25.
- [51] C. Oballe, A. Cherne, D. Boothe, S. Kerick, P. J. Franaszczuk and V. Maroulas, Bayesian topological signal processing, *Discrete & Continuous Dynamical Systems-S*.
- [52] V. Panaretos and Y. Zemel, Statistical aspects of wasserstein distances, *Annual review of statistics and its application*, **6** (2019), 405–431.
- [53] J. A. Perea, A. Deckard, S. B. Haase and J. Harer, Sw1pers: Sliding windows and 1-persistence scoring; discovering periodicity in gene expression time series data, *BMC bioinformatics*, **16** (2015), 1–12.
- [54] J. Power, K. Barnes, A. Snyder, B. Schlaggar and S. Petersen, Spurious but systematic correlations in functional connectivity MRI networks arise from subject motion, *NeuroImage*, **59** (2012), 2142–2154.

- [55] T. Satterthwaite, D. Wolf, J. Loughead, K. Ruparel, M. Elliott, H. Hakonarson, R. Gur and R. Gur, Impact of in-scanner head motion on multiple measures of functional connectivity: relevance for studies of neurodevelopment in youth, *NeuroImage*, **60** (2012), 623–632.
- [56] T. Satterthwaite, D. Wolf, D. Roalf, K. Ruparel, G. Erus, S. Vandekar, E. Gennatas, M. Elliott, A. Smith and H. Hakonarson, Linked sex differences in cognition and functional connectivity in youth, *Cerebral Cortex*, **25** (2015), 2383–2394.
- [57] L. Seversky, S. Davis and M. Berger, On time-series topological data analysis: New data and opportunities, in *Proceedings of the IEEE Conference on Computer Vision and Pattern Recognition Workshops*, 2016, 59–67.
- [58] R. H. Shumway, Time-frequency clustering and discriminant analysis, *Statistics & probability letters*, **63** (2003), 307–314.
- [59] G. Singh, F. Memoli, T. Ishkhanov, G. Sapiro, G. Carlsson and D. Ringach, Topological analysis of population activity in visual cortex, *Journal of Vision*, **8** (2008), 1–18.
- [60] T. Songdechakraiut and M. Chung, Dynamic topological data analysis for functional brain signals, *IEEE International Symposium on Biomedical Imaging Workshops*, **1** (2020), 1–4.
- [61] T. Songdechakraiut and M. Chung, Topological learning for brain networks, *Annals of Applied Statistics*, **17** (2023), 403–433.
- [62] T. Songdechakraiut, L. Shen and M. Chung, Topological learning and its application to multimodal brain network integration, *Medical Image Computing and Computer Assisted Intervention (MICCAI)*, **12902** (2021), 166–176.
- [63] O. Sporns, *Graph Theory Methods for the Analysis of Neural Connectivity Patterns*, 171–185, Springer US, Boston, MA, 2003.
- [64] O. Sporns, G. Tononi and R. Kotter, The human connectome: a structural description of the human brain, *PLoS Computational Biology*, **1**.
- [65] Z. Su, Y. Wang, R. Shi, W. Zeng, J. Sun, F. Luo and X. Gu, Optimal mass transport for shape matching and comparison, *IEEE Transactions on Pattern Analysis and Machine Intelligence*, **37** (2015), 2246–2259.
- [66] Z. Su, W. Zeng, Y. Wang, Z. L. Lu and X. Gu, Shape classification using Wasserstein distance for brain morphometry analysis, in *International Conference on Information Processing in Medical Imaging*, Springer, 2015, 411–423.
- [67] F. Takens, Detecting strange attractors in turbulence, in *Dynamical systems and turbulence, Warwick 1980*, Springer, 1981, 366–381.
- [68] P. Thompson, T. Cannon, K. Narr, T. van Erp, V. Poutanen, M. Huttunen, J. Lonnqvist, C. Standertskjold-Nordenstam, J. Kaprio and M. Khaledy, Genetic influences on brain structure, *Nature Neuroscience*, **4** (2001), 1253–1258.
- [69] N. Tzourio-Mazoyer, B. Landeau, D. Papathanassiou, F. Crivello, O. Etard, N. Delcroix, B. Mazoyer and M. Joliot, Automated anatomical labeling of activations in spm using a macroscopic anatomical parcellation of the MNI MRI single-subject brain, *NeuroImage*, **15** (2002), 273–289.
- [70] P. J. Uhlhaas and W. Singer, Neural synchrony in brain disorders: relevance for cognitive dysfunctions and pathophysiology, *neuron*, **52** (2006), 155–168.
- [71] P. J. Uhlhaas and W. Singer, Abnormal neural oscillations and synchrony in schizophrenia, *Nature reviews neuroscience*, **11** (2010), 100–113.
- [72] S. Ulla, M. Khan and Y.-M. Chu, Majorization theorems for strongly convex functions, *Journal of Inequalities and Applications*, **2019** (2019), 1–13.
- [73] S. Vallender, Calculation of the wasserstein distance between probability distributions on the line, *Theory of Probability & Its Applications*, **18** (1974), 784–786.
- [74] K. van Dijk, M. Sabuncu and R. Buckner, The influence of head motion on intrinsic functional connectivity MRI, *NeuroImage*, **59** (2012), 431–438.
- [75] D. Van Essen, K. Ugurbil, E. Auerbach, D. Barch, T. Behrens, R. Bucholz, A. Chang, L. Chen, M. Corbetta and S. Curtiss, The human connectome project: a data acquisition perspective, *NeuroImage*, **62** (2012), 2222–2231.
- [76] T. Von Oertzen and S. M. Boker, Time delay embedding increases estimation precision of models of intraindividual variability, *Psychometrika*, **75** (2010), 158–175.
- [77] Y. Wang, H. Ombao and M. Chung, Topological data analysis of single-trial electroencephalographic signals, *Annals of Applied Statistics*, **12** (2018), 1506–1534.
- [78] L. Wasserman, Topological data analysis, *Annual Review of Statistics and Its Application*, **5** (2018), 501–532.
- [79] B. C. M. Wijk, C. J. Stam and A. Daffertshofer, Comparing brain networks of different size and connectivity density using graph theory, *PloS one*, **5** (2010), e13701.

- [80] A. Winkler, G. Ridgway, G. Douaud, T. Nichols and S. Smith, Faster permutation inference in brain imaging, *NeuroImage*, **141** (2016), 502–516.
- [81] A. Zalesky, A. Fornito, I. Harding, L. Cocchi, M. Yücel, C. Pantelis and E. Bullmore, Whole-brain anatomical networks: Does the choice of nodes matter?, *NeuroImage*, **50** (2010), 970–983.
- [82] Y. Zhang, Persistent homology and sparse Vietoris-Rips filtration.
- [83] E. Zivot and J. Wang, Vector autoregressive models for multivariate time series, *Modeling financial time series with S-PLUS®*, 385–429.
- [84] A. Zomorodian and G. Carlsson, Computing persistent homology, *Discrete and Computational Geometry*, **33** (2005), 249–274.